frontiers | Frontiers in Astronomy and Space Sciences

TYPE Original Research
PUBLISHED 18 December 2023
DOI 10.3389/fspas.2023.1322980

OPEN ACCESS

EDITED BY
Xueshang Feng,
Chinese Academy of Sciences (CAS), China

REVIEWED BY
Paolo Ventura,
Astronomical Observatory of Rome (INAF), Italy
Ding Yuan,
Harbin Institute of Technology, China

*CORRESPONDENCE
A. Ali,
afouad@sci.cu.edu.eg

RECEIVED 17 October 2023
ACCEPTED 27 November 2023
PUBLISHED 18 December 2023

CITATION
Mohery M, Ali A, Khames AA, Snaid S and Mindil A (2023), Exploring the high abundance discrepancy in the planetary nebula IC 4663.
Front. Astron. Space Sci. 10:1322980.
doi: 10.3389/fspas.2023.1322980

Exploring the high abundance discrepancy in the planetary nebula IC 4663

M. Mohery[1], A. Ali[2]*, Aya A. Khames[2], S. Snaid[3] and A. Mindil[1]

[1]Department of Physics, College of Science, University of Jeddah, Jeddah, Saudi Arabia, [2]Astronomy, Space Science and Meteorology Department, Faculty of Science, Cairo University, Giza, Egypt, [3]Department of Astronomy and Space Science, Faculty of Science, King Abdulaziz University, Jeddah, Saudi Arabia

This article presents an in-depth analysis of integral field unit spectroscopy performed on the Galactic planetary nebula (PN) IC 4663, with a primary focus on investigating its physical characteristics, chemical composition, and morphological properties. The examination involved the utilization of a series of emission-line maps representing various elements and ionization zones, allowing for a comprehensive assessment of morphological and ionization structure of IC 4663. The majority of these maps depict an overall elliptical shape, featuring a relatively faint core at the center. Emanating from this core are two distinct and illuminated lobes extending in opposite directions, forming a conspicuous double-lobed configuration. The chemical analysis conducted on IC 4663 has revealed that the PN is rich in both helium and nitrogen, characterized by an N/O ratio exceeding 0.5, classifying it as a Peimbert type I nebula. Furthermore, the presence of a notably intense He II emission line at λ4686, in conjunction with the existence of high-excitation lines within the nebular spectrum, indicate its classification as a high-excitation class nebula. The computation of O^{2+}, N^{2+}, and N^{3+} through optical recombination lines has unveiled extreme abundance discrepancy factors, with values of 39.0 ± 6 for O^{2+} and 37.0 ± 9 for N^{2+} and N^{3+}. These findings suggest the possibility that the central star of IC 4663 may be part of a binary system with a sub-stellar companion, potentially engaged in a common envelope interaction. Recent astrometric data derived from the Gaia mission further indicate a significant likelihood of interaction between the asymptotic giant branch halo of the PN and its surrounding interstellar medium, particularly in the southeast direction.

KEYWORDS

Planetary nebulae: individual IC 4663 - Properties: physical, chemical, kinematic

1 Introduction

Following the depletion of hydrogen and helium as their nuclear fuel in the cores, low- and intermediate-mass stars (1–8 $M_{\odot}$) progress into the asymptotic giant branch (AGB) phase. Towards the tip of the AGB, these stars experience stellar winds, which cause them to shed a considerable amount of their outer layers. This mass loss can occur in the form of a slow, dense wind or more episodic events like stellar pulsations and thermal pulses. The mass loss is a crucial factor in shaping the subsequent evolution of the star and its surrounding environment. When the central star (CS) reaches a sufficiently high temperature

($T_{eff} \geq 25,000$ K), the surrounding circumstellar envelope becomes ionized, resulting in the formation of a planetary nebula (PN, plural PNe). At different spatial scales, PNe exhibits a variety of shapes and structural components, ranging from small-scale low-ionization structures (LISs), e.g., knots, filaments, and jets to large-scale structures, e.g., rims, shells, and haloes (Balick, 1987; Corradi et al., 1996; Balick et al., 1998; Gonçalves et al., 2001). Various theories have been proposed to explain the formation of LISs within PNe, but none of them can fully account for all the distinct forms (Akras and Gonçalves, 2016, & references therein).

The classical model of interacting stellar winds (ISW), proposed by Kwok et al. (1978), successfully explains the symmetrical and round morphology of PNe through the interaction of fast and tenuous post-AGB wind with slow and dense AGB wind. However, it does not provide a comprehensive explanation for the asymmetric, elliptical, and bipolar shapes observed in PNe. These complex shapes suggest the involvement of additional factors influencing the formation and shaping of PNe, including magnetic fields and CS rotation and binarity (Balick and Frank, 2002, & references therein). Extensive research on the interaction between slow and fast winds has demonstrated that non-spherical mass loss during the AGB phase can account for many of the observed PN morphologies and kinematics (Mellema and Frank, 1995, & references therein). Mellema (1996) has offered a concise overview of hydrodynamic modeling of PNe, highlighting the specific observations that these models aim to replicate and presenting the outcomes of various modeling approaches. Furthermore, García-Segura et al. (2022) have conducted a study utilizing 2D hydrodynamical simulations to explore the evolution from a protoplanetary (PPN) phase to a PN in binary systems that have undergone a common-envelope (CE) event. Their findings suggest that these models have the potential to explain a significant portion of PN shapes, including the elliptical and bipolar morphological classes.

The study of chemical enrichment in the universe through PNe offers valuable insights into several key aspects of astrophysics. It allows us to gain a deeper understanding of stellar nucleosynthesis, the origins and distribution of elements within the cosmos, and the tracing of galactic chemical evolution by examining the abundances of various elements across different regions of a galaxy (Faúndez-Abans and Maciel, 1986; Costa et al., 2004; Maciel et al., 2006). These gradients in elemental abundance provide crucial clues regarding the processes of galaxy formation and evolution, as well as the mechanisms responsible for mixing and transporting enriched materials. Furthermore, the study of PNe in distant galaxies provides unique insights into the chemical conditions of the early universe, shedding light on the composition and development of the cosmos during its formative stages (Magrini et al., 2012; Corradi et al., 2015).

In the framework of studying a sample of PNe located towards the bulge of our galaxy, Cavichia et al. (2010) provide a long-slit spectrum for IC 4663. They derived the physical properties and elemental abundances of IC 4663. Following that, a comprehensive analysis of IC 4663 and its associated CS, categorized as having the spectral type [WN3], was conducted by Miszalski et al. (2012). They employed a CMFGEN NLTE model atmosphere to characterize the CS, revealing a very high temperature of T = 140 kK and a fast stellar wind with $v_{\infty} = 1900$ km s^{-1}. To investigate the physical and chemical characteristics of the ionized nebula, they combined optical and UV spectra from archival low-dispersion *IUE* spectra (SWP33946 and LWP13707). The results displayed a chemical abundance pattern relatively similar to solar values, where the blue portion ($\lambda \leq 5,900$ Å) came from the Gemini Multi-Object Spectrograph (GMOS) spectrum, and the red portion was obtained from the work by Cavichia et al. (2010). Additionally, the shape of IC 4663 was explored using three images captured during the GMOS program, employing Hα and [O III] filters with central wavelengths/FWHMs of 656.0/7.2 nm, 499.0/4.5 nm, and 514.0/8.8 nm, respectively. These images revealed an ellipsoidal bubble surrounded by a fainter outer shell, along with the presence of an external AGB halo expanding at a relatively low velocity of 30 km s^{-1}. Notably, the [O III] image indicated a flux enhancement in the AGB halo towards the southeast (SE) of the CS, suggestive of potential interaction with the interstellar medium (ISM). Furthermore, Puspitaningrum and Malasan (2019) developed a photoionization model for IC 4663 using CLOUDY and observational data spanning from optical to far-infrared wavelengths. They determined the properties of the CS by employing the PoWR atmosphere model, which yielded values of $T_{eff} = 125$ kK and $\log g = 6.0$, aligning with the observed data. By comparing the nebular abundances obtained from the model with those predicted by an AGB model and a born-again scenario evolutionary track, they inferred that IC 4663 originated from a progenitor star with a mass of 3 $M_{\odot}$ and Z = 0.02.

Integral Field Unit (IFU) spectroscopy represents a cutting-edge technique in the examination of extended objects such as PNe, H II regions, and galaxies, offering distinct advantages over traditional long-slit spectroscopy methods. This approach allows researchers to study these extended objects in a 2D field of view, providing a comprehensive understanding of their properties. Establishing the correlation between spectra and spatial structures is vital for accurately measuring the physical conditions and understanding the distribution of different ions within PNe. Emission-line and line ratio maps generated through IFU spectroscopy of PNe contribute valuable insights into their ionization structure, morphology, and the underlying physical processes. Previous work by Ali et al. (2016) has highlighted the advantages of IFU spectroscopy in the field of PNe compared to long-slit spectroscopy. Over the last 2 decades, various authors have delved into IFU spectra of Galactic PNe. Notably, our research group has published a series of papers discussing IFU spectroscopy of PNe utilizing the Wide Field Spectrograph (WiFeS) instrument, with examples including Ali et al. (2015), Basurah et al. (2016), Dopita et al. (2017), Ali and Dopita (2019), and Snaid et al. (2023). A review of the existing literature reveals a substantial body of IFU studies conducted on numerous PNe, as demonstrated by the works of Monreal-Ibero et al. (2005), Tsamis et al. (2007), Danehkar et al. (2013), García-Rojas et al. (2022) and Mari et al. (2023).

Systematic investigations of ionized nebulae, such as H II regions and PNe, have revealed that the abundance of heavy element ions derived from optical recombination lines (ORLs) is higher compared to those deduced from collisionally excited lines (CELs) of identical species. The ratio of ORL to CEL abundances is referred to as the abundance discrepancy factor (ADF). In the majority of PNe, the

ADF typically ranges from 2 to 3. However, a small number of Pne exhibit ADF values that are one or two orders of magnitude higher. Wesson et al. (2018) categorize these variances, describing an ADF value below 5 as "normal," values spanning between 5 and 10 as "elevated," and those exceeding 10 as "extreme."

The major goal of this research is to conduct an extensive analysis of IC 4663 through spectroscopic, morphological, and kinematic investigations using IFU spectra. Furthermore, this research investigates the abundance discrepancy observed within PN, along with assessing the probability of the CS existing within a closely orbiting binary system. The article is structured as follows: Section 2 provides a discussion on the observations and data reduction techniques employed. Section 3 presents the morphology and ionization structures observed in the object. Section 4 provides an investigation into the plasma diagnostics, physical conditions, and chemical composition of the PN. Section 5 discusses the probable close binarity of the PN CS. The interaction between the object and the ISM is examined in Section 6. Finally, the conclusion drawn from the research are summarized in the last section.

2 Observations and data reduction

On 17 May 2018, observations of IC 4663 were carried out using the WiFeS instrument (Dopita et al., 2007) mounted on the 2.3-m telescope of the Australian National University (ANU) at Siding Spring Observatory. WiFeS is a robust integral field, dual-beam, concentric, and image-slicing spectrograph that provides a field of view measuring $25'' \times 38''$ with a spatial resolution of 1.0×1.0. The data were collected in low-resolution mode (R~3000), which corresponds to a velocity resolution of 100 km/s. During these observations, the CCD was set up in double binning mode, producing a $4,096 \times 2048$ data format with $1.0''$ pixels in the spatial direction. Observations were conducted simultaneously in two gratings. The B3000 and R3000 gratings used the RT560 dichroic that cuts at 5600 Å. This setup ensures a significant overlap in wavelength coverage between each of the gratings, resulting in continuous wavelength coverage from ~3400 to ~8950Å. The WiFeS observations were summarized in Table 1. The PyWiFeS pipeline (Childress et al., 2014) was used for data reduction. The wavelength scale was calibrated using nighttime observations of the Ne-Ar arc lamp, whereas the nebular fluxes were calibrated using the standard stars HD 111980 and HD 031128.

TABLE 1 The observing log.

Object	No. of frames	Exposure time (s)	Date	Airmass
IC 4663 (PN G346.2-08.2)				
B3000	3	10, 100, 800	05/15/2018	1.19, 1.19, 1.17
R3000	3	10, 100, 800	05/15/2018	1.19, 1.19, 1.17

3 Emission-line maps

In order to investigate the morphology and ionization structure of the PN, we generated a collection of emission-line maps that represent various elements and ionization states. The majority of these maps exhibit an overall elliptical shape, with a relatively faint core positioned in the central region. Emerging from this core, two distinct and prominently illuminated lobes extend in opposite directions, forming a clear double-lobed structure, and are enveloped by a relatively smooth and extended gas shell. Figure 1 displays three images of the PN, highlighting emission lines of Hα (left panel), He II (middle panel), and [O III] (right panel). Notably, the brightness of the pair of lobes varies across these images. The [O III] map shows brighter lobes compared to the Hα map, which, in turn, is brighter than the He II map. This variation in brightness is attributed to differences in the line fluxes of the three ions. Furthermore, the south lobe in the He II map appears brighter than the north one.

In Figure 2, we have constructed three emission-line maps: [Ar III] (left panel), [Ar IV] (middle panel), and [Ar V] (right panel), with the aim of examining the ionization stratification of the nebula. As expected, the lower ionization line map displays a larger nebular size. The order of the panels, from left to right, corresponds to displaying the argon line maps in ascending order of ionization levels, starting with [Ar III] and progressing to [Ar V]. Notably, the figure reveals that in the emission line of [Ar III], the north lobe appears brighter than the south lobe. However, in the emission lines of [Ar IV] and [Ar V], the north lobe appears relatively dimmer in comparison to the south lobe. This observed variation in brightness across different ionization levels shows the complex ionization structure of the nebula.

Figure 3 displays the nebula in ORLs of nitrogen and oxygen: N II (left panel), O II (middle panel), and O III (right panel). The ORLs lines on nitrogen and oxygen appear less distinct than their corresponding CELs due to their lower fluxes.

4 Physical and chemical analysis

4.1 Global spectra and line fluxes

The software QFitsView v3.3[1] was used to extract the complete spectrum of the PN from the data cubes. A circular aperture of radius $12''$ was used to match the apparent size of the PN. The spectra from the B and R gratings were combined using the scombine task of the IRAF software. The global spectrum of IC 4663 is displayed in Figure 4.

The ALFA code (Wesson, 2016) facilitated the identification and flux measurement of emission lines across the entire spectrum. To calculate the interstellar reddening coefficient, $c(H\beta)$, an iterative method was employed based on the average ratios of the Hydrogen Balmer lines Hα, Hβ, Hγ, and Hδ. This calculation assumed Case B conditions at $T_{eff} = 10,000$ K and relied on the

1 A FITS file viewer using the QT widget library developed at the Max Planck Institute for Extraterrestrial Physics by Thomas Ott.

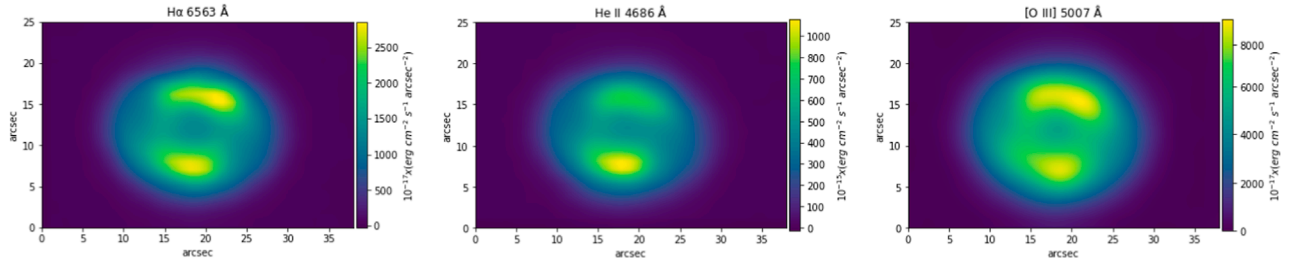

FIGURE 1
The emission-line maps of IC 4663 in three different ions: Hα at 6563 Å, He II at 4686 Å, and [O III] at 5007 Å. The elliptical morphology is seen in all maps. In all figures the North is to the top of the image and East is to the left. The colour bar displays the surface brightness variation of the nebula.

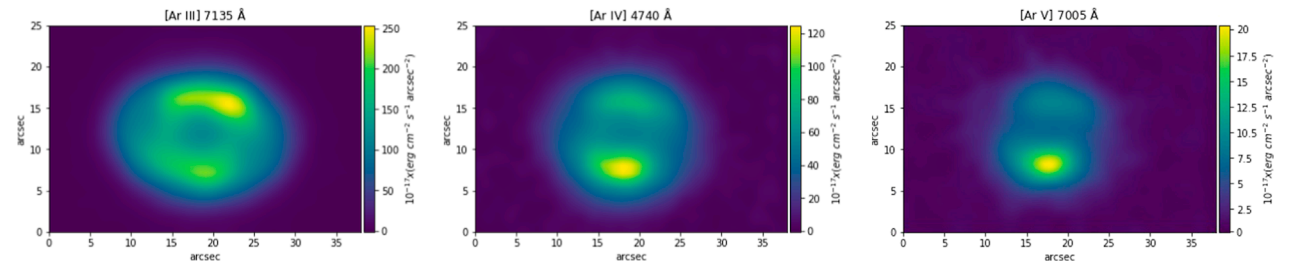

FIGURE 2
The purpose of the three emission-line maps of IC 4663 is to emphasize the ionization stratification of the nebula using different argon ions. The left, middle, and right panels highlight [Ar III] at 7135 Å, [Ar IV] at 4740 Å, and [Ar V] at 7005 Å, respectively. It is apparent that the size of the nebula decreases as we transition from the lower ionization represented by the [Ar III] emission-line map to the higher ionization indicated by the [Ar IV] emission-line map.

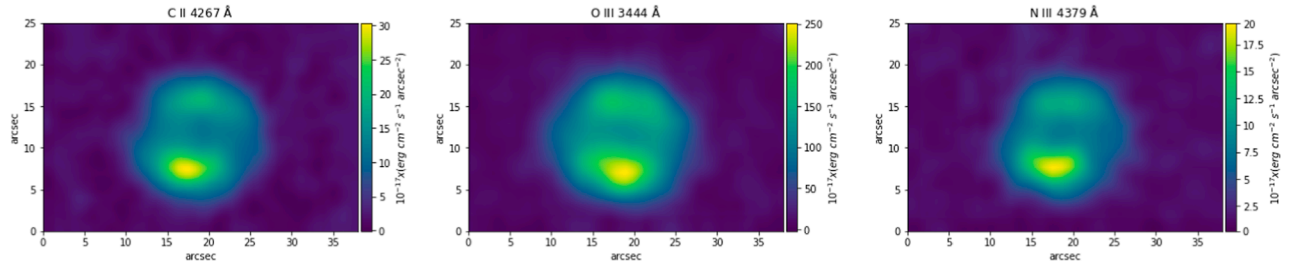

FIGURE 3
The emission-line maps of IC 4663 in three ORLs of C II at 4267 Å (left panel), O III at 3444 Å (middle panel), and N III at 4379 Å (right panel).

Nebular Empirical Abundance Tool [NEAT, Wesson et al. (2012)] The observed line fluxes in the given context were adjusted for interstellar reddening using the extinction law proposed by Howarth (1983). Table 2 provides values for both the observed line fluxes, $F(\lambda)$, and the de-reddened line fluxes, $I(\lambda)$, with respect to Hβ being set at 100. To address statistical uncertainties arising from line flux measurements, NEAT incorporated the Monte Carlo technique, which ensured accurate consideration of these uncertainties throughout subsequent steps of plasma diagnosis, including the determination of physical conditions and chemical abundances.

The line list presented in Table 2 demonstrates that IC 4663 exhibits a significant array of ORLs. Surprisingly, the flux measurements of these lines are observed to be substantially higher compared to analogous lines commonly observed in the majority of PNe. To illustrate this, the corrected fluxes for particular lines, such as O III lines at λ3444.1, N II at λ4026.1, O II at λ4641.8, C II at λ4267.2, and N III at λ4640.6, yield values of 33.3, 2.5, 8.5, 3.0, and 8.7, respectively, relative to F(Hβ) = 100. This finding serves as an indicator of the high ADF of this PN.

Additionally, the spectral analysis indicates that the intensities of low-ionization emission lines, including as [O I], [N I], [O II], and

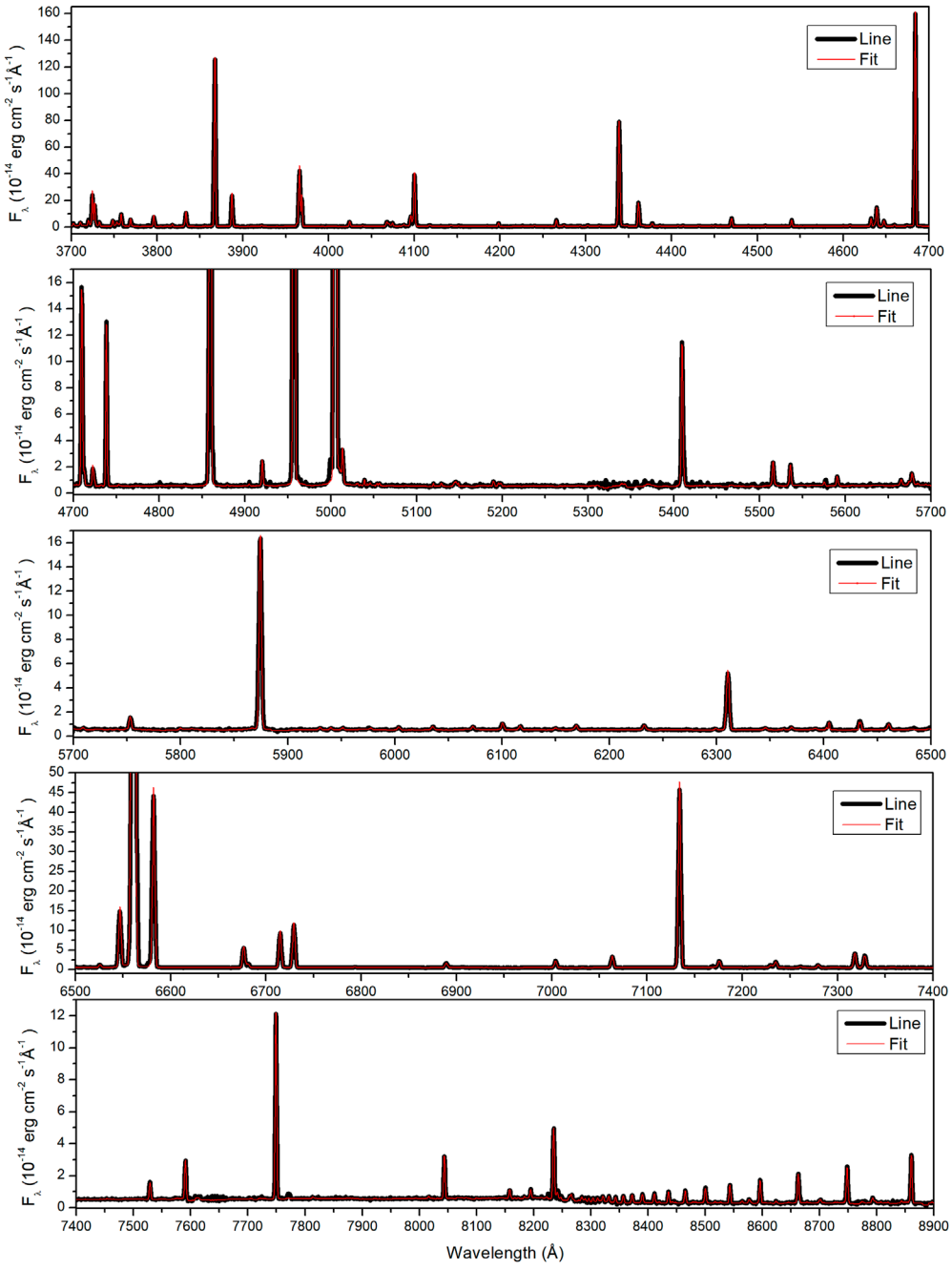

FIGURE 4
The overall spectrum of PN IC 4663. The observed spectrum was represented by the bold black line, while the fitted spectrum obtained using the ALFA code is represented by the thin red line.

[N II], are weak. Particularly, the flux ratio of [N II] λ6583 to Hα is below 0.5. This observation implies that the nebula is nearly optically thin.

The presence of the He II line at λ4686 in the nebular spectrum suggests that the nebula falls into the medium to high excitation class, and its CS has an effective temperature greater than 85 kK. By applying the procedure outlined by Reid and Parker (2010), a high EC value of 10.8 was derived. This value aligns with the presence of highly excited lines like [Ar V] and [Ne IV], which possess atomic ionization energies of 75.0 and 97.1 eV, respectively.

The systemic velocity RV_{sys} of IC 4663 was measured using the ALFA code, primarily from strong emission lines. The heliocentric radial velocity RV_{hel} was then calculated by correcting RV_{sys} for the effect of Earth's motion. The result is -80.0 ± 22.0 km/s, which is consistent with the value reported by Beaulieu et al. (1999). Table 3 provides a comparison, highlighting the differences between the values of $c(H\beta)$, Hα and Hβ fluxes, EC, and RV_{hel}

for IC 4663 and the corresponding values reported in the existing literature.

4.2 Temperatures and densities of IC 4663

The detected emission lines (CELs and ORLs) in the PN spectrum were utilized to determine electron densities and temperatures at various ionization levels. Nebular densities were calculated by employing line ratios: [O II] (λ3727/λ3729), [S II] (λ6716/λ6731), [Cl III] (λ5517/λ5537), and [Ar IV] (λ4711/λ4740). On the other hand, nebular temperatures were calculated using line ratios: [O III] (λ4959 + λ5007)/λ4363, [Ar III] (λ7135 + λ7751)/λ5192, [N II] (λ6548 + λ6584)/λ5754, [O II] (λ7319 + λ7330)/(λ3726 + λ3729), [S II] (λ6717 + λ6731)/(λ4068 + λ4076), and He I (λ7281/λ6678).

According to García-Rojas et al. (2022), in certain highly-excited PNe with high ADFs, the auroral [O III] λ4363 line may be significantly excited by recombination processes, which makes the T_e [O III] diagnostic unreliable (Gómez-Llanos et al., 2020). Additionally, they found that the recombination contribution to the auroral [N II] λ5755 line can strongly impacts the measured line flux in PNe with high ADF. To address these complexities, the analysis incorporated the adjustment of CELs by considering the contribution of ORLs using NEAT, which offers an option to subtract the effect of recombination contribution from key diagnostic CELs.

TABLE 2 Integrated $F(\lambda)$ and de-reddened $I(\lambda)$ line fluxes (relative to Hβ = 100) for IC4663. The complete table is available as **Supplementary Material**.

$\lambda_{Lab.}$(Å)	$\lambda_{Obs.}$(Å)	Ion	$F(\lambda)$	$I(\lambda)$
4711.37	4709.66	[Ar IV]	7.24 ± 0.108	$7.60^{+0.115}_{-0.115}$
4724.15	4722.43	[Ne IV]	1.00 ± 0.020	$1.03^{+0.021}_{-0.021}$
4725.62	4723.90	[Ne IV]	0.36 ± 0.020	$0.40^{+0.021}_{-0.021}$
4740.17	4738.45	[Ar IV]	5.73 ± 0.078	$6.11^{+0.082}_{-0.082}$
4859.32	4857.53	He II	4.17 ± 0.840	$4.62^{+0.847}_{-0.836}$
4861.33	4859.54	H I	100 ± 0.840	$100^{+0.845}_{-0.845}$
4921.93	4920.12	He I	0.83 ± 0.065	$0.92^{+0.064}_{-0.064}$
4958.91	4957.08	[O III]	367 ± 3.35	$354.0^{+3.00}_{-3.00}$
5006.84	5005.02	[O III]	1088 ± 6.98	$1030^{+10.00}_{-10.00}$
5015.68	5013.85	He I	1.36 ± 0.058	$1.24^{+0.055}_{-0.055}$

TABLE 3 The physical parameters of IC 4663, which are derived from its global spectrum.

Parameters	Ours	Literature
log F(Hβ)	−11.42	−11.47 ± 0.03 (1)
C(Hβ)	$0.54^{+0.031}_{-0.031}$	0.58 (2), 0.51 (3)
RV_{hel} (km/s)	−79.7 ± 21.9	−48.7 ± 6 (4), −52.1 ± 6.2 (5), −74 (6)
EC	10.8	7.0 (6)
Peimbert class	Type I	
Ionic density (N_e) in cm^{-3}		
[O II]	2410^{+570}_{-810}	
[S II]	1800^{+280}_{-340}	3810 (2), 1000 (3)
[Cl III]	712^{+325}_{-351}	
[Ar IV]	844^{+178}_{-183}	
Ionic temperature (T_e) in K		
[O II]	14900^{+1600}_{-1800}	12800 (2), 10300 (3)
[S II]	9370^{+1040}_{-1170}	
[N II]	12300^{+400}_{-400}	
[O III]	11400^{+100}_{-100}	11500 (2), 11500 (3)
[Ar III]	10700^{+300}_{-300}	
He I (λ7281/λ6678)	12300^{+900}_{-900}	11400 (3)

(1) Cahn et al. (1992), (2) Cavichia et al. (2010), (3) Miszalski et al. (2012), (4) Schneider and Terzian (1983), (5) Durand et al. (1998), (6) Beaulieu et al. (1999).

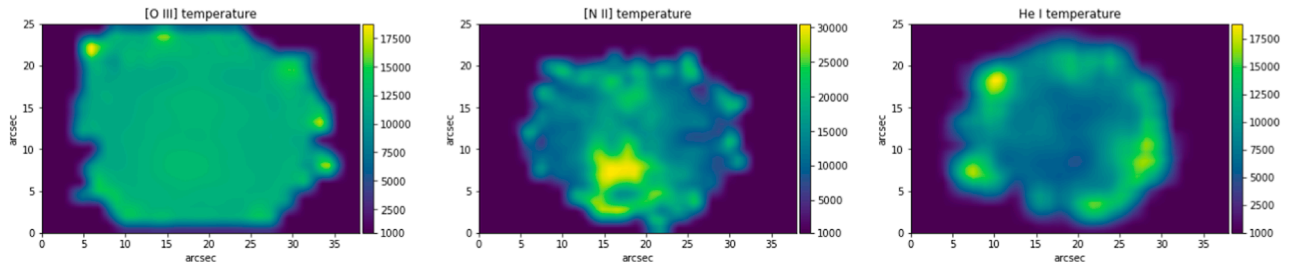

FIGURE 5
The electron temperature of IC 4663 was determined using three different diagnostic line ratios. The temperature map derived from the [O III] diagnostic line ratio is displayed in the left panel, the [N II] line ratio in the middle panel, and the He I line ratio in the right panel.

10.3389/fspas.2023.1322980

TABLE 4 Ionic and total abundances of IC 4663.

Ions	IC 4663
CEL abundances	
N^+/H	$(1.33^{+0.12}_{-1.04}) \times 10^{-6}$
ICF(N)	$(195.00^{+116.00}_{-42.00})$
N/H	$(2.55^{+0.66}_{-0.46}) \times 10^{-4}$
O^0/H	$(2.87^{+2.87}_{-2.80}) \times 10^{-9}$
O^+/H	$(1.77^{+0.25}_{-2.80}) \times 10^{-6}$
O^{2+}/H	$(2.86^{+0.27}_{-0.31}) \times 10^{-4}$
ICF(O)	$(1.56^{+0.02}_{-0.02})$
O/H	$(4.51^{+0.41}_{-0.48}) \times 10^{-4}$
Ne^{2+}/H	$(7.83^{+0.88}_{-1.04}) \times 10^{-5}$
Ne^{4+}/H	$(1.29^{+0.24}_{-0.27}) \times 10^{-5}$
ICF(Ne)	$(1.38^{+0.01}_{-0.01})$
Ne/H	$(1.26^{+0.14}_{-0.17}) \times 10^{-4}$
Ar^{2+}/H	$(1.82^{+0.15}_{-0.17}) \times 10^{-6}$
Ar^{3+}/H	$(1.60^{+0.15}_{-0.18}) \times 10^{-6}$
Ar^{4+}/H	$(1.52^{+0.14}_{-0.16}) \times 10^{-7}$
ICF(Ar)	$(1.38^{+0.04}_{-0.03})$
Ar/H	$(4.93^{+0.42}_{-0.47}) \times 10^{-6}$
S^+/H	$(9.16^{+0.91}_{-5.52}) \times 10^{-8}$
ICF(S)	$(289.00^{+172.00}_{-63.00})$
S/H	$(2.61^{+0.84}_{-0.44}) \times 10^{-5}$
Cl^+/H	$(2.44^{+0.19}_{-1.36}) \times 10^{-9}$
Cl^{2+}/H	$(9.72^{+0.90}_{-1.03}) \times 10^{-8}$
Cl^{3+}/H	$(7.83^{+0.66}_{-0.74}) \times 10^{-8}$
ICF(Cl)	$(1.00^{+0.00}_{-0.00})$
Cl/H	$(1.78^{+0.15}_{-0.17}) \times 10^{-7}$
RL abundances	
He^+/H	$(6.90^{+0.30}_{-0.30}) \times 10^{-2}$
He^{2+}/H	$(6.59^{+0.04}_{-0.04}) \times 10^{-2}$
He/H	$(1.35^{+0.03}_{-0.03}) \times 10^{-1}$
C^{2+}/H	$(2.74^{+0.07}_{-0.07}) \times 10^{-3}$
C^{3+}/H	$(4.97^{+0.67}_{-0.66}) \times 10^{-4}$

(Continued on the following page)

TABLE 4 (*Continued*) Ionic and total abundances of IC 4663.

Ions	IC 4663
ICF(C)	$(1.62^{+0.04}_{-0.04})$
C/H	$(5.25^{+0.16}_{-0.16}) \times 10^{-3}$

Table 3 presents the electron densities and temperatures of IC 4663, comparing them to values documented in previous studies. The findings indicate that the density determined from the [S II] emission line is higher than the value reported by Miszalski et al. (2012), but lower than the value provided by Cavichia et al. (2010). In terms of temperature, the values obtained from the [O III] and He I line ratios are consistent with those reported in the literature, falling within the uncertainty limits. However, the temperature derived from the [O II] diagnostic line ratio is notably higher than the corresponding values found in previous studies.

Figure 5 illustrates the electron temperature distribution of IC 4663 using three different diagnostic line ratios. In the left panel, the temperature map derived from the [O III] diagnostic ratio is shown, revealing a uniform temperature distribution across the PN, ranging from ~9.0 kK to 18.0 kK. Some regions along the PN's border exhibit higher temperatures. In the middle panel, the temperature map derived from the [N II] diagnostic line ratio is presented, showing a slightly higher temperatures compared to the [O III] map, with a range of ~9.0 kK to 30.0 kK. Notably, the highest temperature region corresponds to the lower middle part of the PN, aligning with the location of the southern lobe. The right panel showcases the electron temperature derived from the He I line ratio. This map demonstrates a decrease in temperature from the outer to inner regions of the PN, with temperature values ranging from ~20.0 kK to 5.0 kK. This finding consistent with high-abundance discrepancy factor PNe, which can be attributed to the presence of two obvious gas phases. The inner region exhibits low temperatures and high metal content, while the outer region displays warmer temperatures and normal metal content, as highlighted by García-Rojas et al. (2022).

However, it is important to note that due to the poor signal-to-noise ratios, an accurate map of the distribution of interstellar extinction coefficients across the complete PN could not be generated.

4.3 Ionic and elemental abundances

Table 4 provides the calculated ionic and elemental abundances of IC 4663 using the NEAT code. The abundances of nitrogen, oxygen, neon, argon, sulfur, and chlorine were determined through the analysis of CELs, while the abundances of helium and carbon were derived from the ORLs. The ionic abundances were computed by considering the appropriate temperature and density values for their specific ionization zones. In situations where multiple lines were observed for the same ion, the average abundance was calculated. The elemental abundances were obtained by applying the ionization correction factors (ICFs) reported by Delgado-Inglada et al. (2014) to the calculated ionic abundances.

TABLE 5 Comparison between elemental abundances of IC 4663 and prior studies, Type I PNe, and Sun.

Element	Ours	Cavichia et al. (2010)	Miszalski et al. (2012)	Type I PN (8)	Sun (9)
He/H	0.136	0.111	0.111	0.111	0.1
C/H	5.25E-03		1.58E-04 (4)	2.69E-04	2.69E-04
N/H	2.55E-04	3.09E-04 (1)	1.82E-04 (5)	5.25E-04	6.76E-05
O/H	4.51E-04	6.92E-04 (2)	5.01E-04 (5)	4.47E-04	4.90E-04
Ne/H	1.26E-04	1.78E-04 (1)	1.29E-04 (4)	1.23E-04	8.51E-05
Ar/H	4.93E-06	7.41E-06 (3)	2.69E-06 (6)	2.63E-06	2.51E-06
S/H	2.61E-05	1.07E-05 (1)	1.05E-05 (7)	8.13E-06	1.32E-05
Cl/H	1.78E-07		3.16E-07 (7)		3.16E-07
N/O	0.57	0.45	0.36	1.17	0.14

References of ICFs, and the sun and Orion nebula abundances: (1) Kingsburgh and Barlow (1994), (2) Torres-Peimbert and Peimbert (1977), (3) de Freitas Pacheco et al. (1993), (4) Miszalski et al. (2012), (5) Aller (1984), (6) Barker (1980), (7) Koeppen et al. (1991), (8) Kingsburgh and Barlow (1994), (9) Asplund et al. (2009).

Table 5 presents a comparison of the total abundances of IC 4663 with Type I PNe, solar abundances, and values reported in the literature. The results show a noticeable increase in He, C, and N and slightly increase in Ne, Ar, and S abundances compared to solar values. However, these elevated values are in good agreement with the abundances observed in Type I PNe. The differences in abundance measurements between our analysis and those of Cavichia et al. (2010) and Miszalski et al. (2012) can be attributed to two factors. Firstly, we used ICFs provided by Delgado et al. (2014), while Cavichia et al. (2010) and Miszalski et al. (2012) have used ICFs that determined from many different sources (see Table 5). Secondly, our analysis was based on IFU spectra of IC 4663, while the previous both studies were relied on long-slit spectra.

The PN IC 4663 displays remarkable enrichments of helium (He/H ≥0.125) and nitrogen [log (N/H) + 12 ≥8.0], along with an N/O ratio ≥0.5. These characteristics classify IC 4663 as a Type I PN according to the classification scheme introduced by (Peimbert and Torres-Peimbert, 1983). This classification suggests that the progenitor star of IC 4663 had initial mass ≥3.0 M⊙ (Quireza et al., 2007). In addition to determining the nitrogen and oxygen abundances from the CELs, the analysis also included their calculations from ORLs, specifically O^{2+}/H^{+}, N^{2+}/H^{+}, and N^{3+}/H^{+}. The O^{2+}/H^{+} abundance was derived from the V1, V2, V5, V10, V19, V20, and V48b multiplets, which exhibited consistent agreement with each other. Similarly, the N^{2+}/H^{+} abundances were determined from the V3, V28, and V39b multiplets, while the N^{3+}/H^{+} abundances were obtained from the V2 multiplet.

Table 6 presents the fractional ionic abundances of O II, N II, and N III, along with the averages of each multiplet. To calculate the abundance of each multiplet, an abundance-weighted average of its components was computed, and the full abundances were determined as the average of the multiplet abundances. To assess the abundance discrepancy, two key factors were defined. The ADF (O^{2+}) was determined as the ratio of the ORL abundance of O^{2+} to the CEL abundance of O^{2+}. Similarly, the ADF (N) was calculated as the ratio of the ORL abundances of N^{2+} and N^{3+} to the total nitrogen abundance derived from the CELs. The resulting abundance discrepancy factors are presented in Table 6 for both oxygen and nitrogen. They reveal an extreme abundance discrepancy for both oxygen and nitrogen in IC 4663, with an ADF(O^{2+}) of approximately 39.0 ± 6 and an ADF (N) of approximately 37.0 ± 9. It is worth noting that the derived ADF for oxygen is considered more reliable than that of nitrogen. This is due to the fact that the ORL nitrogen abundance is mainly determined from the N^{2+} and N^{3+} abundances, while the nitrogen abundance from the CELs relies solely on N^{+} lines and heavily depends on the estimated ICF. The accuracy of the ICF becomes particularly uncertain for CELs where only a small fraction of nitrogen is in the form of N^{+}.

These high ADF values observed for oxygen and nitrogen place IC 4663 among the group of PNe with extreme ADFs (ADF > 10) such as A 46, Fg 1, Hf 2-2, and Pe 1–9 (Wesson et al., 2018). According to the findings of Wesson et al. (2018), extreme abundance discrepancy in any PN is indicative of a binary CS. However, this hypothesis also suggests that the presence of a binary CS is insufficient to account for extreme ADFs.

5 Is the CS of IC 4663 part of a close binary system?

The CS of IC 4663 has been classified as a nitrogen Wolf-Rayet [WN] type, making it the first star of this particular class to be identified within PNe. The CS's spectrum exhibits broad emission lines associated with He II and NV, while lacking prominent lines from He I and C IV, placing it with the [WN3] subtype. Observations conducted by Miszalski et al. (2012) revealed radial velocity (RV) variability in the range of 3–4 km/s^{-1}. They concluded that the CS is not in a binary system with a main-sequence or white dwarf companion because in such a binary system the RV variability must be ≳ 5–10 km/s^{-1}, corresponding to a period ≲ 1 day. Additionally, they attributed this minor variability to either noise or wind turbulence affecting the line profiles in the CS spectrum.

TABLE 6 Fractional ionic abundances of O^{2+}, N^{2+}, and N^{3+} lines in IC 4663.

λ(Å)	Multiplet	$\frac{X(line)}{H^+}$	λ(Å)	Multiplet	$\frac{X(line)}{H^+}$
O^{2+}/H^+			N^{2+}/H^+		
4641.81	V1	2.94E-02 ± 5.50E-04	5666.63	V3	1.54E-03 ± 1.25E-04
4649.13	V1	1.30E-02 ± 1.00E-03	5676.02	V3	1.55E-03 ± 5.10E-04
4661.63	V1	3.52E-03 ± 2.70E-04	5679.56	V3	1.51E-03 ± 1.35E-04
4676.23	V1	4.50E-03 ± 5.65E-04	5686.21	V3	1.16E-03 ± 5.35E-04
		1.26E-02 ± 3.25E-04	5710.77	V3	2.48E-03 ± 6.05E-04
4345.55	V2	1.60E-02 ± 1.20E-02			1.65E-03 ± 1.95E-04
4349.43	V2	3.67E-03 ± 4.10E-04	5931.78	V28	2.66E-03 ± 2.45E-04
		9.84E-03 ± 6.00E-03	5941.65	V28	7.68E-04 ± 7.55E-05
4414.9	V5	1.40E-02 ± 1.00E-03			1.71E-03 ± 1.28E-04
4416.97	V5	1.99E-03 ± 4.65E-04	4026.08	V39b	5.80E-02 ± 4.00E-03
4452.38	V5	2.20E-02 ± 9.00E-03	4041.31	V39b	1.40E-02 ± 4.00E-03
		1.27E-02 ± 3.02E-03			3.60E-02 ± 2.83E-03
4069.62	V10	1.30E-02 ± 1.00E-03			
4072.15	V10	4.34E-03 ± 5.00E-04	N^{3+}/H^+		
4075.86	V10	1.10E-02 ± 1.00E-03	4366.89	V2	1.70E-02 ± 2.00E-03
4078.84	V10	1.00E-03 ± 1.00E-03	4640.64	V2	2.25E-03 ± 3.00E-05
		7.34E-03 ± 4.51E-04			9.63E-03 ± 1.00E-03
4153.3	V19	1.90E-03 ± 3.20E-04			
4156.53	V19	6.00E-03 ± 4.00E-03			
		3.95E-03 ± 2.01E-03			
4110.79	V20	5.00E-03 ± 2.00E-03			
4119.22	V20	9.00E-03 ± 2.00E-03			
		7.00E-03 ± 1.41E-03			
4083.9	V48b	2.00E-03 ± 2.00E-03			
4097.26	V48b	5.30E-02 ± 1.00E-02			
		2.75E-02 ± 5.10E-03			
O^{2+}/H^+		**1.13E-02 ± 1.26E-03**	N^{2+}/H^+ & N^{3+}/H^+		**9.36E-03 ± 7.52E-04**
ADF		**39.44 ± 5.94**	ADF		**36.69 ± 8.58**

The weighted mean values were denoted using boldface formatting.

Soker (1997) proposed that the axisymmetric shapes of PNe, such as bipolar and elliptical morphologies, are a consequence of the axisymmetric mass loss experienced by progenitor stars during their interaction with binary companions. These companions can take the form of either stellar or sub-stellar objects, including planets and brown dwarfs. Based on this hypothesis, PNe were categorized into four distinct classes: 1) Progenitors that did not undergo any interaction with their companions; 2) Progenitors that interacted with stellar companions but did not go through a CE phase; 3) Progenitors that interacted with stellar companions through a CE phase; 4) Progenitors that interacted with sub-stellar companions through a CE phase (56% of the PN sample). In accordance with this classification, IC 4663 was assigned to class 4), implying that the morphology of IC 4663 is a result of its progenitor star being part of a close binary system with a sub-stellar companion. The criteria proposed this class also provide an explanation for the presence of spherical halos observed around certain elliptical PNe, as observed in the case of IC 4663 (see Figure 5 in Miszalski et al. (2012)). In their analysis of TESS light curves, Aller et al. (2020) examined eight PNCSs to uncover potential binary systems. Except for one case, they identified evident signs of variability in all of them. The light curves displayed a pattern of variability consistent with an irradiation effect, and two of the targets exhibited ellipsoidal variability. Their findings indicate that the observed variability limits the potential companion to either a very low-mass main-sequence star or a sub-stellar object. In the case where the companion to the CS is a sub-stellar object, it is conceivable for it to display slight variability, as reported in the study by Miszalski et al. (2012).

Sub-stellar objects, such as Jupiter-type exoplanets, are known to have RV variations that range from a few meters per second to considerably higher values. Particularly, in systems where massive gas giants orbit their host stars at close distances, these RV variations can span from a few meters per second up to hundreds of meters per second (Tala Pinto et al., 2020; Hara and Ford, 2023).

In the context of IC 4663, the detection of minor RV variability identified by Miszalski et al. (2012), together with its classification as a class (4) PN by Soker (1997), and the correlation established by Wesson et al. (2018) linking high-ADF PNe to CS binarity, all support the hypothesis of a sub-stellar companion in a common envelope phase with the CS of IC 4663.

To investigate the potential binarity of the PNCS, we thoroughly examined various photometric databases, including the Gaia, Kepler, and TESS missions. Unfortunately, our search did not yield any positive results confirming the presence of a companion. Consequently, further monitoring of the CS is imperative to conclusively determine whether a companion to the PNCS exists or not.

6 IC 4663 interaction with ambient ISM

A spherical AGB halo surrounding IC 4663 was detected in the [O III] image taken by the Gemini South GMOS. The halo displayed an enhancement positioned approximately 22″ SE of the CS. The origin of this enhancement is attributed to the interaction between the PN and the ISM. Wareing et al. (2007) characterized this specific case of interaction as the initial evolutionary phase of interaction between PNe and ISM employing the triple wind model for this description. It should be noted that this phase, the ionised PN remains unaffected by the interaction. Notably, IC 4663 exhibits similar characteristics to the cases of NGC 2438, NGC 2440, NGC 3242, and IC 4593 (Ali et al., 2012).

Following the procedure provided by Mohery et al. (2022), we determined a position angle (PA) for the proper motion of the CS, measuring 171 ± 45. Despite the slightly high uncertainty, primarily caused by a significant error in the μ_α component, this discovery strongly supports the possibility that the observed enhancement in the AGB halo results from its interaction with the ISM. To calculate the PA, we utilized proper motion measurements obtained from the Gaia Data Release 3 (Gaia DR3), which included $\mu_\alpha = -0.0787 \pm -0.0787$ and $\mu_\delta = -0.0787 \pm 0.052469$, along with a photo-geometric distance of 2400^{+557}_{-320} pc determined by Bailer-Jones et al. (2021).

7 Conclusion

In this study, we conducted the first integral field spectroscopy of the southern PN IC 4663, spanning the optical range of 3400–8950 Å. The analysis of the emission-line maps, encompassing low, intermediate, and high ionisation lines, consistently revealed an elliptical shape with two inner illuminated lobes extending in opposite directions from the faint core. This formation created a distinct double-lobed structure. The emission maps, whether from CELs or ORLs, shared a similar overall morphology. However, disparities were noted in the brightness of the lobes and the apparent size of the PN in the CEL and ORL emission-line maps. Moreover, our study confirmed the interaction between IC 4663 and its surrounding ISM by calculating the position angle of CS's motion towards the interaction region.

Spectral analysis of the PN has identified it is a high excitation class object that is nearly optically thin. Furthermore, the Doppler shift observed in the emission lines yielded a heliocentric radial velocity of −80.0 ± 22.0 km/s, which aligns with the values reported in literature. Our measurements of the electron temperature and density of the PN, derived from different diagnostic lines across various ionization stages, are consistent with the previous studies. The electron temperature maps generated for [O III] and [N II] reveal a uniform distribution across the PN, with the exception of slightly higher temperatures observed in the lower middle section of the PN for [N II]. In contrast, the constructed He I map demonstrates a temperature gradient, declined from the outer to inner regions of the PN, thus suggesting the presence of two different gas phases: a cooler inner region and a comparatively warmer outer region. This temperature profile is consistent with what is typically observed in PNe with high ADFs.

Based on the derived elemental abundances of helium, nitrogen, and oxygen, we classified IC 4663 as a Peimbert type I PN, suggesting a progenitor star with a mass larger than 3.0 M⊙. The elemental abundances of the PN show good agreement with those of Type I PNe, exceeding solar abundances. Additionally, there were slight variations in these elemental abundances compared to values reported in the literature. Furthermore, a substantial discrepancy was observed between the oxygen and nitrogen abundances calculated from ORLs versus those from CELs, with a factor of

approximately 40. This categorizes IC 4663 as a PN with extreme ADFs.

The hypothesis of a close binary system within IC 4663, comprising the CS and a sub-stellar companion, is supported by several key observations: (1) the detection of minor radial velocity variability in the CS of IC 4663 CS, (2) the progenitor star of IC 4663 has been categorized as part of a close binary system that underwent interaction with sub-stellar companions during a common envelope phase, and (3) the correlation between high ADFs in PNe and close binary CS systems.

Data availability statement

The original contributions presented in the study are included in the article/Supplementary Material, further inquiries can be directed to the corresponding author.

Author contributions

MM: Formal Analysis, Writing–original draft, Funding acquisition, Methodology. AA: Formal Analysis, Writing–original draft, Data curation, Investigation, Writing-review and editing. AAK: Formal Analysis, Investigation, Data curation, Methodology. SS: Formal Analysis, Investigation, Writing–original draft. AM: Formal Analysis, Funding acquisition.

Funding

The author(s) declare financial support was received for the research, authorship, and/or publication of this article. This work was funded by the University of Jeddah, Jeddah, Saudi Arabia under grant No. (UJ-23-DR-249). Therefore, the authors thank the University of Jeddah for its technical and financial support.

Acknowledgments

This work was funded by the University of Jeddah, Jeddah, Saudi Arabia under grant No. (UJ-23-DR-249). Therefore, the authors thank the University of Jeddah for its technical and financial support. We express our gratitude to the referees for their careful examination of our work and valuable feedback and suggestions, which have significantly enhanced the quality of the paper. This work presents results from the European Space Agency (ESA) space mission Gaia. Gaia data are being processed by the Gaia Data Processing and Analysis Consortium (DPAC).

Conflict of interest

The authors declare that the research was conducted in the absence of any commercial or financial relationships that could be construed as a potential conflict of interest.

Publisher's note

Supplementary material

The Supplementary Material for this article can be found online at: https://www.frontiersin.org/articles/10.3389/fspas.2023.1322980/full#supplementary-material

References

Akras, S., and Gonçalves, D. R. (2016). Low-ionization structures in planetary nebulae - I. Physical, kinematic and excitation properties. *MNRAS* 455, 930–961. doi:10.1093/mnras/stv2139

Ali, A., Amer, M. A., Dopita, M. A., Vogt, F. P. A., and Basurah, H. M. (2015). The physics and kinematics of the evolved, interacting planetary nebula PN G342.0-01.7. *MNRAS* 583, A83. doi:10.1051/0004-6361/201526223

Ali, A., and Dopita, M. A. (2019). IFU spectroscopy of southern PNe - VII. Photoionization modelling of intermediate excitation class objects. *MNRAS* 484, 3251–3266. doi:10.1093/mnras/stz201

Ali, A., Dopita, M. A., Basurah, H. M., Amer, M. A., Alsulami, R., and Alruhaili, A. (2016). IFU spectroscopy of southern planetary nebulae - III. *MNRAS* 462, 1393–1404. doi:10.1093/mnras/stw1744

Ali, A., Sabin, L., Snaid, S., and Basurah, H. M. (2012). Interacting planetary nebulae: I. Classification and orientation⋆. *A&A* 541, A98. doi:10.1051/0004-6361/201118389

Aller, A., Lillo-Box, J., Jones, D., Miranda, L. F., and Barceló Forteza, S. (2020). Planetary nebulae seen with TESS: discovery of new binary central star candidates from Cycle 1. *A&A* 635, A128. doi:10.1051/0004-6361/201937118

Aller, L. H. (1984). *Physics of thermal gaseous nebulae*. Berlin, Germany: Springer. doi:10.1007/978-94-010-9639-3

Asplund, M., Grevesse, N., Sauval, A. J., and Scott, P. (2009). The chemical composition of the sun. *ARA&A* 47, 481–522. doi:10.1146/annurev.astro.46.060407.145222

Bailer-Jones, C. A. L., Rybizki, J., Fouesneau, M., Demleitner, M., and Andrae, R. (2021). Estimating distances from parallaxes. V. Geometric and photogeometric distances to 1.47 billion stars in Gaia early data Release 3. *AJ* 161, 147. doi:10.3847/1538-3881/abd806

Balick, B. (1987). The evolution of planetary nebulae. I. Structures, ionizations, and morphological sequences. *AJ* 94, 671. doi:10.1086/114504

Balick, B., Alexander, J., Hajian, A. R., Terzian, Y., Perinotto, M., and Patriarchi, P. (1998). FLIERs and other microstructures in planetary nebulae. IV. Images of elliptical PNs from the [ITAL]hubble[/ITAL] [ITAL]space[/ITAL] [ITAL]T[/ITAL] [ITAL]elescope[/ITAL]. *AJ* 116, 360–371. doi:10.1086/300429

Balick, B., and Frank, A. (2002). Shapes and shaping of planetary nebulae. *ARA&A* 40, 439–486. doi:10.1146/annurev.astro.40.060401.093849

Barker, T. (1980). The ionization structure of the ring nebula. I. Sulfur and argon. *ApJ* 240, 99–104. doi:10.1086/158210

Basurah, H. M., Ali, A., Dopita, M. A., Alsulami, R., Amer, M. A., and Alruhaili, A. (2016). Problems for the WELS classification of planetary nebula central stars: self-consistent nebular modelling of four candidates. *MNRAS* 458, 2694–2709. doi:10.1093/mnras/stw468

Beaulieu, S. F., Dopita, M. A., and Freeman, K. C. (1999). A survey of planetary nebulae in the southern galactic bulge. *ApJ* 515, 610–632. doi:10.1086/307052

Cahn, J. H., Kaler, J. B., and Stanghellini, L. (1992). A catalogue of absolute fluxes and distances of planetary nebulae. *A&AS* 94, 399–452.

Cavichia, O., Costa, R. D. D., and Maciel, W. J. (2010). Planetary nebulae in the inner Milky Way: new abundances. *Rev. Mex. Astron. Astrofis.* 46, 159–177. doi:10.48550/arXiv.1003.0416

Childress, M. J., Vogt, F. P. A., Nielsen, J., and Sharp, R. G. (2014). PyWiFeS: a rapid data reduction pipeline for the Wide field spectrograph (WiFeS). *Ap&SS* 349, 617–636. doi:10.1007/s10509-013-1682-0

Corradi, R. L. M., Kwitter, K. B., Balick, B., Henry, R. B. C., and Hensley, K. (2015). The chemistry of planetary nebulae in the outer regions of M31. *ApJ* 807, 181. doi:10.1088/0004-637X/807/2/181

Corradi, R. L. M., Manso, R., Mampaso, A., and Schwarz, H. E. (1996). Unveiling low-ionization microstructures in planetary nebulae. *A&A* 313, 913–923.

Costa, R. D. D., Uchida, M. M. M., and Maciel, W. J. (2004). Chemical abundances of planetary nebulae towards the Galactic anticenter. *A&A* 423, 199–207. doi:10.1051/0004-6361:20034539

Danehkar, A., Parker, Q. A., and Ercolano, B. (2013). Observations and three-dimensional ionization structure of the planetary nebula SuWt 2. *MNRAS* 434, 1513–1530. doi:10.1093/mnras/stt1116

de Freitas Pacheco, J. A., Barbuy, B., Costa, R. D. D., and Idiart, T. E. P. (1993). Type I planetary nebulae in the Large Magellanic Cloud: oxygen, sulphur and argon abundances as tracers of chemical enrichment. *A&A* 271, 429–434.

Delgado-Inglada, G., Morisset, C., and Stasińska, G. (2014). *In revista Mexicana de astronomia y astrofisica conference series*, 17–17.

Dopita, M. A., Ali, A., Sutherland, R. S., Nicholls, D. C., and Amer, M. A. (2017). IFU spectroscopy of southern planetary nebulae IV: a physical model for IC 418. *MNRAS* 470, 839–864. doi:10.1093/mnras/stx1166

Dopita, M., Hart, J., McGregor, P., Oates, P., Bloxham, G., and Jones, D. (2007). Astrophys. *Space Sci.* 310, 255.

Durand, S., Acker, A., and Zijlstra, A. (1998). The kinematics of 867 galactic planetary nebulae. *A&AS* 132, 13–20. doi:10.1051/aas:1998356

Faúndez-Abans, M., and Maciel, W. J. (1986). Galactic abundance gradients from planetary nebulae. *Rev. Mex. Astron. Astrofis.* 12, 240–248.

García-Rojas, J., Morisset, C., Jones, D., Wesson, R., Boffin, H. M. J., Monteiro, H., et al. (2022). MUSE spectroscopy of planetary nebulae with high abundance discrepancies. *MNRAS* 510, 5444–5463. doi:10.1093/mnras/stab3523

García-Segura, G., Taam, R. E., and Ricker, P. M. (2022). Common-envelope shaping of planetary nebulae - IV. From protoplanetary to planetary nebula. *MNRAS* 517, 3822–3831. doi:10.1093/mnras/stac2824

Gómez-Llanos, V., Morisset, C., García-Rojas, J., Jones, D., Wesson, R., Corradi, R. L. M., et al. (2020). The impact of strong recombination on temperature determination in planetary nebulae. *MNRAS* 498, L82–L86. doi:10.1093/mnrasl/slaa131

Gonçalves, D. R., Corradi, R. L. M., and Mampaso, A. (2001). Low-ionization structures in planetary nebulae: confronting models with observations. *ApJ* 547, 302–310. doi:10.1086/318364

Hara, N. C., and Ford, E. B. (2023). Statistical methods for exoplanet detection with radial velocities. *Annu. Rev. Statistics Its Appl.* 10, 623–649. doi:10.1146/annurev-statistics-033021-012225

Howarth, I. D. (1983). LMC and galactic extinction. *MNRAS* 203, 301–304. doi:10.1093/mnras/203.2.301

Kingsburgh, R. L., and Barlow, M. J. (1994). Elemental abundances for a sample of southern galctic planetary nebulae. *MNRAS* 271, 257–299. doi:10.1093/mnras/271.2.257

Koeppen, J., Acker, A., and Stenholm, B. (1991). Spectrophotometric survey of southern planetary nebulae. II. Chemical compositions. *A&A* 248, 197.

Kwok, S., Purton, C. R., and Fitzgerald, P. M. (1978). On the origin of planetary nebulae. *ApJ* 219, L125–L127. doi:10.1086/182621

Maciel, W. J., Lago, L. G., and Costa, R. D. D. (2006). New results on the time variation of the radial abundance gradients from planetary nebulae. *Proc. Int. Astronomical Union* 2 (S234), 453–454. doi:10.1017/S174392130600370X

Magrini, L., Stanghellini, L., and Gonçalves, D. R. (2012). Extragalactic planetary nebulae: tracers of the chemical evolution of nearby galaxies. *Planet. Nebul. Eye Future* 283, 251–258. doi:10.1017/S1743921312011040

Mari, M. B., Akras, S., and Gonçalves, D. R. (2023). Low-ionization structures in planetary nebulae - III. The statistical analysis of physico-chemical parameters and excitation mechanisms. *MNRAS* 525, 1998–2014. doi:10.1093/mnras/stad2256

Mellema, G. (1996). Hydrodynamic models of planetary nebulae. *Ap&SS* 245, 239–253. doi:10.1007/BF00642229

Mellema, G., and Frank, A. (1995). Radiation gasdynamics of planetary nebulae - V. Hot bubble and slow wind dynamics. *MNRAS* 273, 401–410. doi:10.1093/mnras/273.2.401

Miszalski, B., Crowther, P. A., De Marco, O., Köppen, J., Moffat, A. F. J., Acker, A., et al. (2012). IC 4663: the first unambiguous [WN] Wolf-Rayet central star of a planetary nebula. *MNRAS* 423, 934–947. doi:10.1111/j.1365-2966.2012.20929.x

Mohery, M., Ali, A., Mindil, A., and Alghamdi, S. A. (2022). Interacting planetary nebulae III: verification and galactic population based on the measurements of Gaia EDR3. *Ap&SS* 367, 63. doi:10.1007/s10509-022-04085-y

Monreal-Ibero, A., Roth, M. M., Schönberner, D., Steffen, M., and Böhm, P. (2005). Integral field spectroscopy of faint halos of planetary nebulae. *ApJ* 628, L139–L142. doi:10.1086/432664

Peimbert, M., and Torres-Peimbert, S. (1983). "Type I planetary nebulae,". *Planetary nebulae*. Editor D. R. Flower (London, U.K: IAU Symposium), 233–241.

Puspitaningrum, E., and Malasan, H. L. (2019). Photoionization modelling of the Wolf-Rayet planetary nebulae IC 4663 based on multiwavelength observations. *J. Phys. Conf. Ser.* 1231, 012031. doi:10.1088/1742-6596/1231/1/012031

Quireza, C., Rocha-Pinto, H. J., and Maciel, W. J. (2007). Bayesian posterior classification of planetary nebulae according to the Peimbert types. *A&A* 475, 217–231. doi:10.1051/0004-6361:20078087

Reid, W. A., and Parker, Q. A. (2010). An evaluation of the excitation-class parameter for the central stars of planetary nebulae. *PASA* 27, 187–198. doi:10.1071/AS09055

Schneider, S. E., and Terzian, Y. (1983). Planetary nebulae and the galactic rotation curve. *ApJ* 274, L61–L64. doi:10.1086/184151

Snaid, S., Ali, A., and Alruhaili, A. (2023). Comprehensive study of the galactic planetary nebula NGC 2792. *Ap&SS* 368, 62. doi:10.1007/s10509-023-04218-x

Soker, N. (1997). Properties that cannot Be explained by the progenitors of planetary nebulae. *ApJS* 112, 487–505. doi:10.1086/313040

Tala Pinto, M., Reffert, S., Quirrenbach, A., Stock, S., Trifonov, T., and Mitchell, D. S. (2020). Precise radial velocities of giant stars. XIV. Evidence of planetary companions around HD 25723, 17 Sco, 3 Cnc, and 44 UMa. *A&A* 644, A1. doi:10.1051/0004-6361/202038285

Torres-Peimbert, S., and Peimbert, M. (1977). Photoelectric photometry and physical conditions of planetary nebulae. *Rev. Mex. Astron. Astrofis.* 2, 181–207.

Tsamis, Y. G., Walsh, J. R., Pequignot, D., Barlow, M. J., Liu, X.-W., and Danziger, I. J. (2007). Integral-field spectroscopy of galactic planetary nebulae with VLT FLAMES. *Messenger* 127, 53.

Wareing, C. J., Zijlstra, A. A., and O'Brien, T. J. (2007). The interaction of planetary nebulae and their asymptotic giant branch progenitors with the interstellar medium. *MNRAS* 382, 1233–1245. doi:10.1111/j.1365-2966.2007.12459.x

Wesson, R. (2016). ALFA: an automated line fitting algorithm. *MNRAS* 456, 3774–3781. doi:10.1093/mnras/stv2946

Wesson, R., Jones, D., García-Rojas, J., Boffin, H. M. J., and Corradi, R. L. M. (2018). Confirmation of the link between central star binarity and extreme abundance discrepancy factors in planetary nebulae. *MNRAS* 480, 4589–4613. doi:10.1093/mnras/sty1871

Wesson, R., Stock, D. J., and Scicluna, P. (2012). Understanding and reducing statistical uncertainties in nebular abundance determinations. *MNRAS* 422, 3516–3526. doi:10.1111/j.1365-2966.2012.20863.x